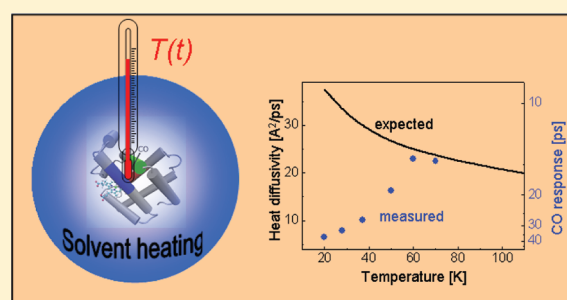


Temperature Dependence of the Heat Diffusivity of Proteins

Jan Helbing,[†] Michael Devereux,^{||} Karin Nienhaus,[‡] G. Ulrich Nienhaus,^{‡,§} Peter Hamm,^{†,*} and Markus Meuwly^{||,*}[†]Physikalisch-Chemisches Institut, Universität Zürich, Winterthurerstrasse 190, CH-8057 Zürich, Switzerland^{*}Institute of Applied Physics and Center for Functional Nanostructures (CFN), Karlsruhe Institute of Technology, Wolfgang-Gaede-Strasse 1, D-76131 Karlsruhe, Germany[§]University of Illinois at Urbana–Champaign, 1110 West Green Street, Urbana, Illinois 61801, United States^{||}Department Chemie, Universität Basel, Klingelbergstrasse 80, CH-4056 Basel, Switzerland

S Supporting Information

ABSTRACT: In a combined experimental–theoretical study, we investigated the transport of vibrational energy from the surrounding solvent into the interior of a heme protein, the sperm whale myoglobin double mutant L29W-S108L, and its dependence on temperature from 20 to 70 K. The hindered libration of a CO molecule that is not covalently bound to any part of the protein but is trapped in one of its binding pockets (the Xe4 pocket) was used as the local thermometer. Energy was deposited into the solvent by IR excitation. Experimentally, the energy transfer rate increased from $(30 \text{ ps})^{-1}$ at 20 K to $(8 \text{ ps})^{-1}$ at 70 K. This temperature trend is opposite to what is expected, assuming that the mechanism of heat transport is similar to that in glasses. In order to elucidate the mechanism and its temperature dependence, nonequilibrium molecular dynamics (MD) simulations were performed, which, however, predicted an essentially temperature-independent rate of vibrational energy flow. We tentatively conclude that the MD potentials overestimate the coupling between the protein and the CO molecule, which appears to be the rate-limiting step in the real system at low temperatures. Assuming that this coupling is anharmonic in nature, the observed temperature trend can readily be explained.



1. INTRODUCTION

Heat transport across heme proteins has, in the past, been investigated extensively.^{1–4} Vibrational energy flow from the heme group in hemoglobin or myoglobin into the surrounding solvent could be directly followed using ultrafast spectroscopy because electronic relaxation very quickly converts the energy of an absorbed visible photon into vibrational energy of the heme, leading to an initial local temperature jump of several hundred Kelvin.² Both the cooling of the heme and the heating of the surrounding solvent have been investigated. Two distinct time constants of less than 10 ps and approximately 20 ps are typically found in these experiments. Hochstrasser and co-workers have interpreted the slower time scale observed for solvent heating as a signature of diffusive heat transport across the bulk protein,² in agreement with early MD simulations.⁵ The faster time scale, however, was initially attributed to a non-diffusive process due to collective motions of the protein. Indeed, while the structural order in proteins is generally too local to give rise to truly delocalized phenomena, it is significantly larger than that of liquids or glasses, leading to speculations about the connection between efficient heat transport and biologically relevant signaling pathways.^{6–8}

On the basis of more recent MD simulations, however, it has been suggested that fast energy transport from a photoexcited heme to the surrounding solvent predominantly goes through

the propionate side chains,⁹ which are part of the heme moiety and connect it directly to the protein surface. Even without this particular difficulty, distinguishing contributions from local equilibration of the chromophore and transport across the bulk protein is not straightforward in experiments based on heme excitation. When described by heat transport theory, essentially two interfaces, between heme and protein and between protein and solvent, have to be taken into account.³

In order to reduce complexity and to address the heat transport problem in polypeptides in a site-selective way, the vibrational energy transport through model peptide helices was recently studied by transient IR spectroscopy with the help of systematic isotope labeling.^{10–13} These works showed that vibrational excitation spreads essentially along the backbone of the polymer without a significant contribution from structure-forming hydrogen bond interactions. Model calculations revealed that low frequency, delocalized vibrational modes can favor fast propagation of an (external) perturbation. The rate-limiting step for the

Special Issue: Femto10: The Madrid Conference on Femtochemistry

Received: June 30, 2011

Revised: October 21, 2011

Published: November 02, 2011

propagation of energy, however, is very often the local equilibration of vibrational excitation, governed by the coupling between high-frequency localized and low-frequency delocalized modes.^{14,15}

In the light of these findings, in this work, we revisit the problem of energy dissipation in a globular protein with three major modifications: (i) we study the process of heating the molecule via the solvent from the outside; (ii) we probe temperature via the kinetic (librational) energy of a CO molecule that is trapped in a cavity near the center of the protein, but that is *not* covalently bound to any part of the protein; and (iii) we perform the experiment at different low temperatures where the influence of protein-specific delocalized vibrational modes should be most pronounced. To that end, we choose the myoglobin (Mb) double mutant L29W-S108L since it has been shown that a dissociated CO remains trapped exclusively in the Xe4 pocket at temperatures below ~ 80 K.¹⁶ The experiments are complemented by MD simulations, which help us to address the different rate-determining steps in the energy transfer process in detail.

2. MATERIALS AND METHODS

2.1. Experimental Procedures. The procedure and setup for this experiment has been described in detail in ref 17. Purified sperm whale Mb double mutant L29W-S108L was dissolved at a concentration of ~ 20 mM in a 75% glycerol/25% potassium phosphate (v/v) buffer mixture at pH 8.0. The sample was reduced with a sodium dithionite solution and stirred under an atmosphere of $^{13}\text{C}^{18}\text{O}$. A few microliters of the sample solution was sandwiched between two 2 mm thick CaF_2 windows separated by a 75 μm mylar spacer inside a vibration-reduced closed cycle cryostat.

At a temperature between 80–90 K, approximately 70% of the CO molecules were photodissociated from the heme iron and trapped in the Xe4 pocket of Mb by nanosecond laser irradiation at 532 nm.¹⁶ This resulted in an optical density for the CO molecules trapped in the Xe4 pocket of 5–7 mOD (at 20 K) on top of a broad solvent background.

The mid-infrared femtosecond (fs) laser pulses of ~ 100 fs duration and 150 cm^{-1} bandwidth were centered at 2020 cm^{-1} . They were produced by difference frequency mixing of signal and idler from a double stage optical parametric amplifier.¹⁸ For the pump–probe measurements, a small portion of the mid-IR beam (4%) was split off to produce probe and reference pulses. The main portion of the beam (1.8–2.0 $\mu\text{J}/\text{pulse}$) passed a delay stage and a $\lambda/2$ plate for polarization control. After passing the sample, probe and reference beams were dispersed in a spectrometer and imaged onto a MCT (mercury cadmium telluride) double array detector with 2 cm^{-1} resolution. At pump–probe delays between 1 and 10 ps, a strong background arising from interference of the probe beam with scattered pump laser light strongly perturbed the very weak signals and could not be sufficiently suppressed by delay time dithering (except for one measurement series performed at 20 K). Data points between 1 and 10 ps were therefore disregarded.

2.2. Molecular Dynamics Simulations. Molecular dynamics (MD) simulations were carried out using the NAMD program¹⁹ with the CHARMM22 force field.²⁰ The initial MbCO protein structure was taken from an equilibrated L29F mutant with CO already present inside the Xe4 pocket.²¹ The Phe29 side chain of the L29F mutant was then replaced by Trp, and the side chain of Ser108 was replaced by Leu to generate the L29W-S108L double

mutant used in the experiment (Figure 1a). The protein was solvated in a box with dimensions $63 \times 55 \times 58\text{ \AA}$ resulting in a system of 2545 protein atoms and 9064 water molecules. Water molecules were treated with a TIP3P potential.²² Electrostatic and van der Waals interactions were evaluated up to a cutoff distance of 12 \AA , with a switching function used between 10 and 12 \AA to smooth truncation. Periodic boundary conditions were applied. Simulations were performed at 20, 50, 75, and 100 K. A separate 5 ns NVT equilibration was performed at each temperature, followed by a further 5 ns NVE simulation to generate 250 starting structures at 20 ps intervals. The 250 stored sets of coordinates and velocities for each temperature were then modified by scaling the velocities of water molecule atoms by a factor 1.5. The scaled velocities cause solvent heating, representative of the laser pulse used to perturb the solvent in the experiment described above. The resulting 500 sets of starting coordinates and velocities at each temperature (250 each for $\lambda = 1.0$ and $\lambda = 1.5$) were used to run 20 ps trajectories at each of the four different temperatures. At 20 and 100 K, the temperature jump is ~ 2 and ~ 6 K, respectively. A total of 2000 20 ps trajectories were therefore performed. Two hundred fifty trajectories for each set of starting conditions were found to be sufficient to detect CO heating. In trials averaged over fewer trajectories, the small changes in CO dynamics associated with solvent heating could not be distinguished from the background noise caused by random CO motions and collision events in each simulation. Trajectories were analyzed by calculating the thermal kinetic energy of the CO molecule

$$\bar{E} = \frac{N}{2} k_{\text{B}} T_{\text{CO}} \quad (1)$$

where N is the number of degrees of freedom (6 in an unconstrained diatomic molecule) and \bar{E} the total kinetic energy of the C and O atoms, averaged over all 250 trajectories. Helix kinetic energies were calculated using all backbone C and N atoms for selected residues forming and surrounding the Xe4 pocket (8 residues in each case, shown in Figure 1a). Exponential and biexponential fits of the response in CO kinetic energy required longer, 250 ps trajectories to obtain reliable asymptotic values. The asymptotic values for CO and the helix kinetic energy ($T(\infty)$) were taken as the average values of the kinetic energy over the final 50 ps of each of the two hundred 250 ps simulations, and the initial kinetic energy $T(0)$ is the averaged value over all trajectories at $t = 0$. For CO, $T(0)$ was included in the fit to capture effects at $t = 0$. Biexponential fits were performed according to

$$T(t) = T(\infty) + c(T(0) - T(\infty))e^{-\alpha_1 t} + (1 - c)(T(0) - T(\infty))e^{-\alpha_2 t} \quad (2)$$

Fitted values were obtained for the coefficient c and exponents α_1 and α_2 . Error bars for the time constants were obtained from bootstrapping. For this, 125 out of the 200 trajectories (250 ps in length) were selected at random. Time constants were fitted using this subset, and a new set of 125 trajectories was selected. This process was repeated 100 times, and the mean and standard deviation of the 100 fitted time constants were evaluated for an error estimate of the fitted values using all 200 trajectories.

The CO kinetic energy was found to lie below that corresponding to the global simulation temperature in many of the unscaled ($\lambda = 1.0$) 20 ps simulations, despite the 5 ns NVT equilibration time. This suggests either weak coupling between

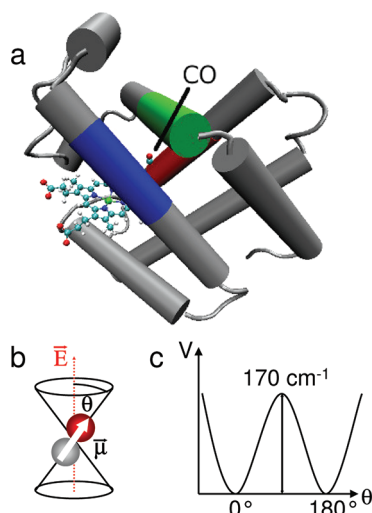


Figure 1. (a) Structure of the Mb mutant L29W. CO is trapped in the Xe4 cavity after photo dissociation from heme at low temperature. Selected residues from helix B (green), E (blue), and G (red) were chosen to monitor the energy transfer from the protein surface to the Xe4 pocket in the MD simulations. (b) The restricted motion of the CO molecule relative to the internal electric field inside the Xe pocket and (c) a model for the potential it experiences.

the high frequency CO stretch and the lower-frequency surrounding protein modes (meaning fluctuations in CO temperature following collision events in the 5 ns NVE simulation persist over many of the restarted trajectories) or anomalies due to simulation conditions as previously observed for SHAKE,²³ the NVE ensemble with periodic boundary conditions,^{24–26} or thermostats during NVT equilibration.²⁷ However, for the following discussion, it is more relevant that it is possible to prepare a well-defined initial state that allows the determination of relative changes in the state of the system upon solvent excitation.

As common for such low-temperature studies, a glycerol/water mixture was used as the solvent in the experiment since it forms an amorphous glass upon freezing, while crystalline ice is likely to perturb the folding of the protein. Since the protein force fields are parametrized for TIP3 water and not for glycerol or glycerol/water mixtures, we chose pure water as the solvent in the simulation study, which will be present in the form of amorphous ice under the simulation conditions. We do not expect this difference to significantly affect the results since glycerol²⁸ and amorphous phases of water²⁹ show very similar thermal properties and, furthermore, since solvent thermalization is not rate-limiting (as we will see).

2.3. Background: Principle of the Local Thermometer. The principle of the local thermometer has been established in refs 16, 17, and 30. In brief, a CO molecule is dissociated from the heme and then diffuses to the Xe4 pocket, also called C-site, located 6 Å above the distal side of the heme (Figure 1a). We study the Mb double mutant L29W-S108L, which is especially well suited for detailed spectroscopic investigations of this particular cavity. It has been shown that CO remains trapped exclusively in the Xe4 pocket at temperatures below $\sim 80 \text{ K}$.¹⁶ Similarly to CO trapped in the primary docking site B after photodissociation,³¹ two preferential CO orientations with respect to a strong electric field in site C (Figure 1b) give rise to a doublet spectrum. The lines narrow and split further as the temperature is lowered (Figure 2a). These observations were successfully explained by a model originally proposed by Gordon.³² It assumes that (inertial) reorientation

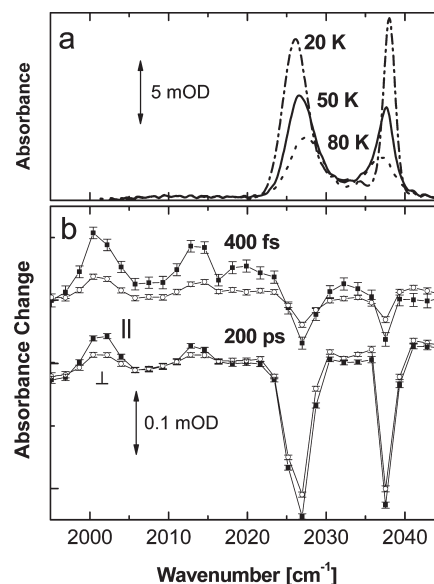


Figure 2. (a) FTIR absorption spectra of $^{13}\text{C}^{18}\text{O}$ in the Xe4 pocket of the Mb double mutant L29W-S108L at 20, 50, and 80 K. (b) Transient absorption spectrum after broad band excitation at a pump–probe delay of 400 fs and 200 ps for a sample initially at 50 K for parallel (black squares) and perpendicular (open circles) polarization of the pump and probe pulse, respectively. Reprinted with permission from ref 17. Copyright 2005 American Institute of Physics.

of the CO molecules is the dominant contribution to the decay of the transition dipole correlation function, $c_1(t) = \langle \vec{\mu}(0) \cdot \vec{\mu}(t) \rangle$. For essentially unrestricted motion, for example, at high temperatures, the absorption spectrum (given by the Fourier transform of $c_1(t)$) is very broad and difficult to detect. When the orientational motion of the molecules is restricted, the fast inertial decay of $c_1(t)$ is incomplete, and the transition dipole correlation function decays biexponentially. Its slow decay component leads to narrow spectral lines, which are easily detectable. Close to quantitative agreement with linear absorption data¹⁶ as well as time-resolved anisotropy data¹⁷ was reached by evaluating the dipole correlation functions for an effective double well potential (Figure 1c),

$$V(\theta) = V_0 \sin^2 \theta \quad (3)$$

where θ is the angle between a protein-fixed axis and V_0 is a barrier of approximately 170 cm^{-1} .¹⁶ With increasing temperature, the amplitude of the CO librational motion increases and the intensity of the narrow spectral lines decreases (Figure 2a). The strong temperature dependence of the intensity of the C=O vibrational mode makes it a very sensitive thermometer, which probes the excitation of the low-frequency librational degrees of freedom of the CO molecule in a very direct and well understood manner.

3. RESULTS

3.1. Experimental Results. In our previous work,¹⁷ we had used polarization-dependent infrared pump–probe spectroscopy to directly observe the orientational motion of CO inside the Xe4 cavity. The critical observable was the anisotropy of the 1–2 transition of the C=O stretch vibration, which gives rise to two

bands about 25 cm^{-1} red-shifted from the fundamentals, due to the anharmonicity of the CO bond (positive bands in Figure 2b).

In the present work, we concentrate on the bleach signals (negative bands in Figure 2b), which appear at the same frequencies as the CO bands in the stationary spectrum (Figure 2a). We see in Figure 2b that the bleach/stimulated emission signals reflect the red-shifted excited state absorption signals at early delay times (400 fs), both in their strength and their anisotropies. This is expected since the intensities as well as the transition dipole moment orientations of the CO ($\nu = 0 \rightarrow (\nu = 1)$ and $(\nu = 1) \rightarrow (\nu = 2)$) transitions are similar for a close-to-harmonic mode. At later delay times (see the 200 ps spectrum in Figure 2b), the excited state absorption slightly decreases due to population relaxation, but surprisingly, the intensity of the bleach strongly increases, which we attribute to heating: in fact, the majority of the broad band laser pulse energy is not absorbed by the CO molecules, but is initially deposited in the surrounding water/glycerol solvent due to the combination band of water (libration and OH bending) that peaks near 2000 cm^{-1} . By comparing the bleach intensity at long pump–probe delays with temperature-dependent FTIR data,¹⁶ we can estimate a temperature jump on the order of 2 K at 70 K and four times larger at 20 K (see the Supporting Information for calibration spectra). This is consistent with the absorbed laser power and the temperature-dependence of the heat capacity of glycerol and the protein and corresponds to an excitation of approximately 10 solvent molecules per protein. In line with this interpretation, hardly any anisotropy is observed at late delay times. The protein itself does not undergo any orientational diffusion; nevertheless, the excited solvent molecules are randomly oriented relative to the proteins. In summary, with the bleach signal, we observe protein-mediated heat transport from the surrounding solvent to the CO molecule, which serves as a local thermometer. Furthermore, the changes in temperature are sufficiently small so that the thermometer can be assumed to be linear over the range of the temperature jump.¹⁶

Figure 3 shows the increase of the bleach signal as a function of time for temperatures between 20 and 70 K. Within signal-to-noise, the response can be adequately fit by a single-exponential function; the resulting time constants are reported in the top inset of Figure 3 as a function of temperature. Heat transport from the surrounding water to the CO cavity becomes more efficient as the temperature is increased.

In order to exclude solvent equilibration as a possible source of the strong temperature dependence of the CO response, we have directly probed absorption changes of the glycerol/water solvent (sample without protein, path length $25\text{ }\mu\text{m}$) near 1600 cm^{-1} after excitation with a laser pulse centered at 2100 cm^{-1} (see Figure 3, bottom). In this probe window, broad absorption bands of both water and glycerol bleach and shift upon heating, making these transient signals sensitive to the changes of solvent temperature. Between 20 and 90 K, the solvent equilibration was found to be temperature-independent with a time constant of 3–4 ps.

3.2. Molecular Dynamics Simulations. All-atom simulations were employed to follow the response of the CO molecule in the Xe4 pocket after heating the solvent molecules surrounding the protein. The simulations allow an analysis of energy transfer from the solvent to the CO molecule mediated by the protein in atomistic detail. The response of the CO molecule to thermal excitation of the solvent was investigated for a range of initial temperatures after scaling all solvent velocities by $\lambda = 1.5$ (see Materials and Methods). CO heating takes place in all

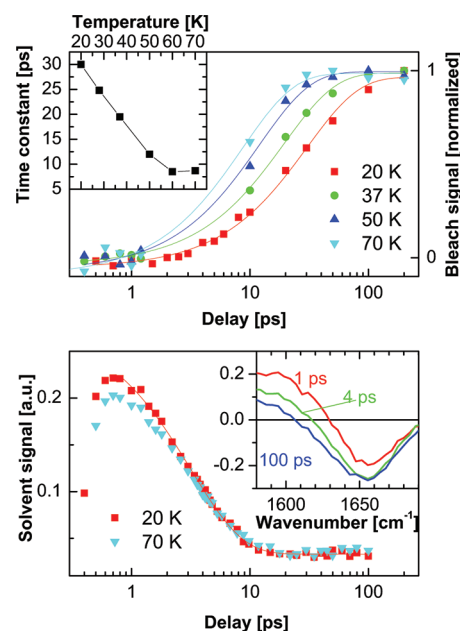


Figure 3. Top: Kinetics of the CO bleach signal (normalized) for various temperatures from 20 to 70 K following excitation of the solvent background. The insert shows the time constants deduced from an exponential fit as a function of temperature. Because of scattering (see Materials and Methods), the time regime between 1 and 10 ps is difficult to access. Bottom: Transient response of a glycerol/water sample near 1600 cm^{-1} at 20 K (squares) and 70 K (triangles) under similar excitation conditions. The inset shows transient spectra at 70 K.

simulations where solvent velocities are scaled, so that the average CO kinetic energy of trajectories with excited solvent is visibly higher than where the solvent velocities are left unperturbed ($\lambda = 1.0$). The rate of energy transfer is rapid. Most of the heating occurs within the first 5 ps, and the CO kinetic energy begins to stabilize over the following 20 ps. An exponential fit of the CO response at 20 and 100 K was performed for the CO kinetic energy averaged over all 250 ps trajectories (Figure 4). Bootstrapping (see Materials and Methods) yielded average time constants of $6 \pm 1\text{ ps}$ and $10 \pm 4\text{ ps}$ at 20 and 100 K, respectively. These results indicate that the CO response time is largely invariant to changes in temperature within the signal-to-noise ratio of the data fitted (and if at all, the temperature trend is opposite to the experimentally observed one).

The rapid time scale of CO heating is of particular interest, as simulations of CO relaxation after vibrational excitation ($[(\nu = 1) \leftarrow (\nu = 0)]$) in Mb³³ as well as experimental measurements^{17,34} demonstrated only weak coupling to the protein environment during cooling, with a decay constant of $T_{10} \approx 600\text{ ps}$. The contrastingly much faster rate of CO heating, therefore, results from energy being transferred into translational and rotational degrees of freedom of CO, rather than vibrational excitation. The translational and rotational modes should couple more efficiently to the surrounding protein via collisions inside the Xe4 pocket, since it matches much better the density of states of a protein.^{35–37}

The data in Figure 4 allows us to investigate possible routes of energy transfer from the protein surface to CO via three helices (B, E, and G; see Figure 1) that form and surround the Xe4 pocket. It shows the average kinetic energy of the backbone atoms selected from each of these helices at around the position of the pocket as a function of simulation time. Averaging was

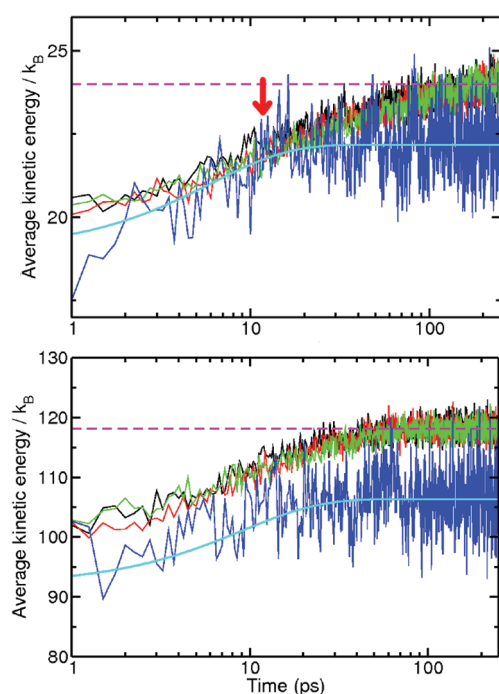


Figure 4. Average kinetic energy (in units of k_B) of the CO molecule and selected helix backbone atoms near the Xe4 cavity (shown in Figure 1a) as a function of simulation time after solvent excitation. The solvent velocity scaling factor used for solvent excitation is $\lambda = 1.5$. Kinetic energies of helix B (black), helix E (red), helix G (green), and the CO molecule (blue) are shown, averaged over 200 independent trajectories, 250 ps in length. Simulations were carried out at (top) 20 K and (bottom) 100 K. The total average kinetic energy of the entire system (including solvent) is shown as a dashed horizontal line for reference. The point where CO kinetic energy overshoots that of the surrounding protein is marked with a red arrow (see text for details). Exponential fits of CO kinetic energy are shown as solid lines in cyan.

again performed over all trajectories at each temperature. The larger number of atoms in each helix allows for more averaging than was possible for the CO molecule and, therefore, gives a better signal-to-noise ratio. It can be seen that heating takes place in all three helices on a similar time scale. This might be expected as all helices are in direct contact with the excited solvent molecules at the protein surface. The similar heating response suggests a roughly isotropic heat flow through the helices. Also included in Figure 4 are the averaged kinetic energies of the entire system, comprising the whole protein and solvent box. This shows that the helices indeed fully thermalize within 250 ps. At 20 K, the helix response occurs on two time scales and is fit as a sum of two exponentials (eq 2). The rapid process (time constants 7, 9, and 7 ps for helices B, E, and G, respectively) is found to contribute more strongly (coefficient $c \approx 0.6$) than the slower process (time constants 56, 59, and 53 ps; coefficient $(1 - c) \approx 0.4$). At 100 K, the response can be well described by a single exponential, yielding time constants of 13, 16, and 15 ps for helices B, E, and G, respectively. For direct comparison with the data at 20 K, fitting the response at 100 K as a double exponential yields a dominant process (coefficients $c \approx 0.7, 0.9$, and 1.0) with time constants 16, 16, and 14 ps) and secondary processes, which contribute significantly less to the fit (coefficients $(1 - c) \approx 0.3, 0.1$, and 0.0) with time constants 5, 15, and 167 ps. In conclusion, the helix response can be described by a rapid process on the

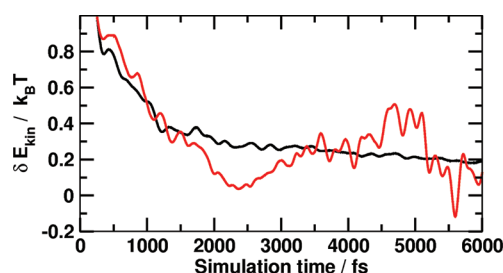


Figure 5. Cooling curves for thermally excited CO at 20 K (black) and 100 K (red). The kinetic energy traces are scaled accordingly to facilitate comparison.

10 ps time scale at 20 and 100 K and a slower process on a 50 ps time scale, which is only visible at low temperatures.

As can be seen in Figure 4, the slope of the initial rise of the CO average kinetic energy coincides with that of the helices. After about 10 ps, however, the CO kinetic energy levels off and remains relatively constant over the subsequent simulation time, whereas the helix kinetic energy continues to rise on a slower time scale. At 20 K, the CO kinetic energy appears to even slightly overshoot. Apparently, the water initially heats only a certain subset of modes of the protein, which in turn efficiently couple to the CO molecule. Presumably, this subset has lower frequency modes since they are resonant with both the water intermolecular degrees of freedom as well as the CO translational and rotational degrees of freedom. Furthermore, low-frequency modes in proteins have a tendency to spatially delocalize over larger regions. As a consequence, they more efficiently transport vibrational energy.^{35–37} However, higher frequency modes of the protein, such as C=O or C–H vibrations, are expected to thermalize on much slower time scales of many tens of picoseconds, in particular at low temperatures (similar to that of the C=O vibration) because the density of states is small in the high-frequency region. Hence, we assume that the slower second component in the time dependence of the helix kinetic energy reflects thermalization of such high-frequency modes of the protein. As energy is then distributed over more degrees of freedom, thermalization of high frequency modes will slightly lower the temperature of the simulation box as a whole, since its heat capacity is finite, explaining the slight overshooting of the CO kinetic energy. The interplay between energy transport through low frequency modes and thermalization of high frequency modes has been described in detail in the context of small helices.³⁸

Energy transfer from the protein to the CO molecule turned out to be difficult to analyze more quantitatively. To more conclusively establish whether this rate is temperature-dependent, the reverse process, i.e., energy dissipation of a thermally excited CO molecule to its environment, was also considered. To this end, MD simulations at 20 and 100 K were carried out in which the CO molecule was excited by increasing the velocity vectors of the C- and O-atom by 25%. Energy dissipation was monitored by following the CO kinetic energy as a function of time and quantified by considering the difference between the unscaled and the scaled trajectory. At 20 and 100 K, a total of 15 trajectories, 10 ps in length, was analyzed. The decrease of the kinetic energy is shown in Figure 5. As can be seen, cooling is essentially complete after 2 ps, and the rates of cooling at 20 and 100 K do not differ substantially. Fitting the relaxation curves with eq 2 yields a relaxation time of 1 ± 0.3 ps at both temperatures. This is significantly faster than the forward rate (~ 10 ps). Thus, energy

transfer between the protein and the CO molecule is not the rate-limiting step as judged from the MD simulation.

4. DISCUSSION

Leitner and co-workers calculated the heat diffusivity D of proteins in analogy to that of glasses.^{35–37} In this theory, the temperature dependence of the heat diffusivity D originates from the temperature dependence of both the thermal conductivity κ and the heat capacity c ³⁵

$$D \equiv \frac{\kappa}{c} = \frac{\int d\omega \rho(\omega)c(\omega)D(\omega)}{\int d\omega \rho(\omega)c(\omega)} \quad (4)$$

where $\rho(\omega)$ is the density of normal modes, $c(\omega)$ is the contribution of a particular normal mode to the total heat capacity (depending on the occupation of a particular normal mode), and $D(\omega)$ is the contribution of that normal mode to energy diffusion. This expression can be interpreted as a weighted sum over all contributions $D(\omega)$ to the total diffusivity, where $\rho(\omega)c(\omega)$ is the weighting factor. Both, thermal conductivity κ and the heat capacity c increase with temperature. However, the heat capacity c increases more strongly and overcompensates the rise of the thermal conductivity κ , so heat diffusivity D is expected to decrease with temperature. This decrease arises from a shift in thermal population from lower frequency modes, which carry energy efficiently since they are typically delocalized over larger spatial areas, to a larger fraction of the population being in higher frequency modes at higher temperatures, which transport energy less efficiently.

In order to relate our results to these thermal properties we assume that we can model heat transport as a diffusion process, and describe the protein as a sphere of radius R_0 with the local CO thermometer essentially in the center. Thermal diffusion inside the sphere is governed by the following equation:³⁹

$$\frac{\partial T(r,t)}{\partial t} = D \frac{1}{r^2} \frac{\partial}{\partial r} \left(r^2 \frac{\partial T(r,t)}{\partial r} \right) \quad (5)$$

When a protein is initially at a temperature T_0 , it approaches the solvent temperature T_∞ according to the general solution

$$\frac{T(r,t) - T_\infty}{T_0 - T_\infty} = \sum_{k=1}^{\infty} \frac{c_k}{\chi} \sin(\gamma_k \chi) \exp\left(-\gamma_k^2 \frac{D}{R_0^2} t\right) \quad (6)$$

where $\chi = r/R_0$, and γ_k and c_k are constants, which depend on boundary conditions (see the Supporting Information). For example, when the outside of the protein is always at the temperature of the solvent ($T(R_0) = T_\infty$), $\gamma_k = k\pi$, and $c_k = (2)/(\pi k)(-1)^{k+1}$.³⁹ Different boundary conditions can lead to smaller values of γ_1 , but the difference to the next larger γ_k is always approximately π , and $c_k \propto 1/k$, so only the leading term in eq 6 contributes, apart from very early times. Consistent with our experiment, the temperature change at the center of the sphere is thus exponential. The time constant

$$\tau = \frac{R_0^2}{\gamma_1^2 D} \quad (7)$$

is inversely proportional to the thermal diffusivity D of the protein.

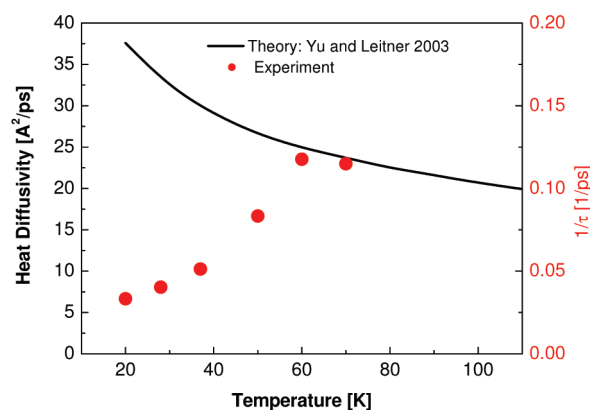


Figure 6. Comparison of the heat diffusivity predicted by Leitner and co-workers³⁵ (black, left scale) with the experimental time constants (red, right scale).

In Figure 6, our experimental data (red circles, right scale) are compared with the theoretical result from Leitner and co-workers (black line, left scale).³⁵ In contrast to the theoretical prediction and in contrast to what is commonly observed for bulk glasses,⁴⁰ the thermal diffusivity $D \propto 1/\tau$ of myoglobin appears to increase with temperature below 60 K. At these temperatures, however, agreement between time-domain data and prediction can be reached using $(R_0/\gamma_1)^2 = 200$. For an effective protein radius, $R_0 = 23$ Å (the radius of a sphere containing the myoglobin mass at the proper density²); this is equivalent to $\gamma_1 = 0.6$, within the range of possible solutions of eq 5. This scaling is also consistent with the time constant (~ 20 ps) found at room temperature for the inverse process, the diffusive heating of water after photo-excitation of heme.²

Temperature enters in eq 4 only through the temperature dependence of the heat capacity $c(\omega)$ of the individual modes of the protein. Leitner's theory is intrinsically quantum-mechanical, so $c(\omega)$ is temperature-dependent

$$c(\omega) = \frac{(\hbar\omega)^2}{k_B T^2} \frac{e^{\hbar\omega/k_B T}}{(e^{\hbar\omega/k_B T} - 1)^2} \quad (8)$$

However, our MD simulation is classical with a constant heat capacity (in the harmonic case)

$$c(\omega) = k_B = \text{const.} \quad (9)$$

We found that the heat diffusivity predicted by the MD simulations is essentially temperature-independent (within signal-to-noise). Analysis of the data at 50 and 75 K showed that within signal-to-noise, this is true for the entire temperature range from 20 to 100 K. Furthermore, at the highest temperatures, the experimental time constants do agree quite well with that of the MD simulations, which yield a rate for CO heating of approximately $(10 \text{ ps})^{-1}$. Hence, both Leitner's theory and our MD simulation actually agree with each other with respect to their temperature dependence, apart from the difference between the classical and a quantum-mechanical heat capacity. Both theories build on the same type of a potential energy surface (i.e., an empirical force field) but differ quite substantially in their approach otherwise. Leitner's theory is inherently a quantum-mechanical picture and is an equilibrium approach that treats anharmonicity perturbatively up to third-order terms of the potential energy surface. In contrast, our MD simulation is a nonequilibrium,

nonperturbative approach, albeit classical in nature. The agreement of both theories is reassuring, and we conclude that they actually describe vibrational energy transport in the protein correctly. If we were to correct our MD results for the quantum occupation numbers (which ultimately give rise to the temperature dependence of the quantum heat capacity, eq 8), it would in fact result in a heat transport rate that decreases with increasing temperature, opposite to our experimental observation.

Hence, although the MD simulations provide insight into heat transport along the helices, they do not provide an atomistic explanation for the temperature dependence of heat transfer from the surrounding to the CO molecule. Possible shortcomings of the MD simulations in correctly capturing the experimentally observed temperature dependence are (A) the thermalization of the solvent itself, (B) the solvent protein interface, or (C) the coupling between the protein and the librational motion of CO inside the Xe4 cavity. In the following sections, these possibilities will be discussed in detail.

4.1. Solvent Thermalization. One possibility is that the experimentally observed temperature dependence reflects solvent thermalization. In the MD simulation, the velocities of all solvent atoms are uniformly scaled in order to mimic the temperature jump, exciting both intra- and intermolecular degrees of freedom. Hence, energy is essentially equipartitioned already when it is deposited. In the experiment, in contrast, absorption is primarily due to the libration–OH bending combination band of the water near 2000 cm^{-1} ; hence, energy is deposited in a mode specific manner. However, the excited water modes have a large spectral overlap with those of glycerol in 1:3 water/glycerol mixture, so water and glycerol are expected to equilibrate rapidly. We indeed observe experimentally that the solvent equilibrates on a few picosecond time scale in an essentially temperature-independent manner (Figure 3).

Furthermore, both glycerol²⁸ and amorphous phases of water (usually forming under pressure)²⁹ show heat transport properties of glasses. Notably, the heat diffusivity decreases with increasing temperature, just as predicted for myoglobin.³⁶ Overall, thermal equilibration within the solvent surrounding the protein should, therefore, not be the rate-limiting step and, if at all, slow down with increasing temperature. This cannot explain the observed acceleration of the CO response with increasing temperature.

4.2. Solvent–Protein Interface. After vibrational excitation of the solvent, the energy has to be transferred to the protein. Therefore, the coupling between solvent and protein modes constitutes an interface that has to be modeled correctly. In the spherical diffusion model, next to the thermal diffusivity D , there is a second parameter γ_1 that influences the observed time-constant of the temperature change at the center of the protein. If we release the restriction $T(R_0) = T_\infty$, the temperature gradient at the interface (and thus γ_1) is determined by the ratio of the so-called heat transfer coefficient and the conductivity of the protein. The heat transfer efficiency would have to increase by a factor of 3–4 faster with temperature than the thermal conductivity in order to explain our observations. This contradicts the observation that the thermal conductivity of glycerol²⁸ is almost the same as that predicted for myoglobin.³⁶ Furthermore, it has been observed by Stock and co-workers¹⁵ that vibrational energy transport rates in polypeptides are extremely insensitive to the exact potentials; energy transport rates are a highly averaged property for which the density of states counts more than the details of MD potentials. The same is true for the glassy solvent, so solvent and protein are thermally relatively homogeneous media.

We thus believe that the vibrational energy transfer through the solvent–protein interface is unlikely to be the rate-limiting step.

4.3. Protein–CO Coupling. The coupling between the protein and the CO molecule might be expected to be weak since (a) it is not covalently bound and (b) the CO per se does not have a large density of states, so details of the interaction potentials might in fact matter. In the following, we describe the coupling between the noncovalently bound CO molecule and its protein environment perturbatively, along the lines of ref 41. To set the stage, we first consider the effect of bilinear coupling, in which case the CO hindered rotational mode would exchange energy only with protein modes that are resonant, $\omega_{\text{pr}} = \omega_{\text{CO}}$. Both classical and quantum mechanical perturbation theory then reveal for the energy transfer rate⁴¹

$$\frac{\partial E_{\text{CO}}}{\partial t} \propto n_{\text{pr}} - n_{\text{CO}} \quad (10)$$

where n_{CO} is the occupation number of the CO mode, and n_{pr} is that of the resonant protein mode(s). If we assume that the CO molecule is initially at a temperature T_0 and the protein at an elevated temperature $T_0 + \Delta T$ with $\Delta T \ll T_0$, the occupation number of the protein can be expanded as

$$\begin{aligned} n_{\text{pr}}(T_0 + \Delta T) &= n_{\text{pr}}(T_0) + \frac{dn_{\text{pr}}}{dT}\Delta T \\ &= n_{\text{pr}}(T_0) + \frac{c_{\text{pr}}(T_0)}{\hbar\omega_{\text{pr}}}\Delta T \end{aligned} \quad (11)$$

where $c_{\text{pr}}(T_0)$ is the heat capacity of the protein mode (eq 8). With these ingredients, we obtain for the energy transfer rate

$$\frac{\partial E_{\text{CO}}}{\partial t} \propto \frac{c_{\text{pr}}(T_0)}{\hbar\omega_{\text{pr}}}\Delta T \quad (12)$$

since we have $n_{\text{pr}}(T_0) = n_{\text{CO}}(T_0)$ for two resonant modes. Finally, since

$$\frac{\partial T_{\text{CO}}}{\partial t} = \frac{1}{c_{\text{CO}}} \frac{\partial E_{\text{CO}}}{\partial t} \quad (13)$$

we find that the temperature dependence cancels

$$\frac{\partial T_{\text{CO}}}{\partial t} \propto \Delta T \quad (14)$$

For bilinear coupling, transport of thermal energy is independent of the initial temperature T_0 . In classical mechanics, where the heat capacity is temperature-independent anyway, we obtain the same result.

For cubic coupling, in contrast, we do obtain a temperature dependence of the heat transfer rate. In this case, we have to consider two resonant processes, with either $\omega_{\text{CO}} = \omega_i + \omega_j$ or $\omega_{\text{CO}} = \omega_j - \omega_i$, respectively, where ω_i and ω_j are protein modes. Quantum-mechanical perturbation theory reveals for the two processes that⁴¹

$$\begin{aligned} \text{(I)} \quad \frac{\partial E_{\text{CO}}}{\partial t} &\propto n_i n_j - n_{\text{CO}} n_j - n_{\text{CO}} n_i - n_{\text{CO}} \\ \text{(II)} \quad \frac{\partial E_{\text{CO}}}{\partial t} &\propto n_i n_j + n_{\text{CO}} n_j - n_{\text{CO}} n_i + n_j \end{aligned} \quad (15)$$

The last terms (n_{CO} and n_j) result from zero-point energy and, hence, are not present in the classical perturbation theory.⁴¹ Along the lines of the derivation above, these expressions can be simplified for the classical case, where $n_i = k_B T / \hbar \omega_i$,

and we obtain

$$\frac{\partial T_{\text{CO}}}{\partial t} \propto \frac{k_{\text{B}} T_0}{\hbar \omega_i \hbar \omega_j} \Delta T \quad (16)$$

for both processes. Quantum-mechanically, the expressions are quite involved but deviate from the classical result only for $k_{\text{B}} T_0 \lesssim 0.2 \hbar \omega$ (the frequency of the hindered rotation of the CO is $\omega_{\text{CO}} \approx 20 \text{ cm}^{-1}$,¹⁶ i.e., for the temperatures of this study, we can use the classical result). In essence, it is the product of occupation numbers in eq 15 that renders the heat transfer rate proportional to the starting temperature T_0 . Consider, for example, process (II). In that case, energy is transferred from mode j to the CO mode, but in order to do so, it requires another protein mode i , the occupation n_i of which scales with temperature T_0 . Higher order processes will scale more strongly with temperature.

Leitner's theory for heat transport in proteins treats the problem on essentially a harmonic level. Harmonic normal modes, equivalent to bilinear coupling in the discussion above, reveal a temperature-independent $D(\omega)$ in eq 4 (the overall temperature dependence enters only through the temperature dependence of the heat capacity, eq 8). An anharmonic correction to Leitner's theory, which indeed is temperature-dependent, does not yet play a significant role in the temperature range of the present study; it leads to a correction of $\lesssim 30\%$ below 100 K.³⁵ What differentiates the CO molecule from the rest of the protein is its potentially very weak coupling to the latter. As such, its librational degrees of freedom stay localized (i.e., they are not part of any delocalized normal mode), and anharmonicity might play a bigger role in a relative sense. Despite the fact that the MD simulations do not reproduce the effect (which they could, conceptually speaking), we believe that it is this coupling that constitutes the rate-limiting step. Assuming that the coupling is dominated by anharmonic terms, the temperature dependence of energy transfer would indeed go in the experimentally observed direction.

The highest temperature point in Figure 6 might indicate that the CO-protein coupling is no longer rate-limiting at temperatures $\gtrsim 60 \text{ K}$ and that the temperature dependence of the overall kinetics turns into that predicted by Leitner's theory.³⁵ Unfortunately, we could not verify that trend since the CO would no longer be stable in the Xe4 pocket at higher temperatures.

One possible reason for the failure of the MD simulations to reproduce the temperature dependence for the thermalization of the CO molecule might lie in the force fields that overestimate the protein–CO coupling (e.g., by too large of a bilinear coupling term). Indeed, in the reverse computer experiment, investigating the cooling after direct heating of the CO molecule, we found a rapid 1 ps temperature-independent equilibration rate for this step. The force field description for the CO molecule that had to be used in the present work clearly has its limitations. As is known from previous work on relaxation of CN^- in water, higher order multipole moments are required to reliably describe energy transfer from the vibrationally excited cyanide ion to the solvent.⁴² In this particular case, even a multipolar representation for the surrounding solvent (water) was required to quantitatively capture vibrational relaxation. In the present case, both the large number of simulations required and the time scale covered by the simulations made it impossible to use such refined models. It remains to be seen whether a better CO model is sufficient to capture the physics or whether even a multipolar representation of the surrounding protein or at least part of it will be needed.

A final reason may be related to the inability of atomistic simulations to capture effects on the few kcal/mol scale quantitatively. In problems related to typical ligand binding changes in activity, measured as rate constants, differ by several orders of magnitude and translate into free energy differences of $\sim 10 \text{ kcal/mol}$. Given that relative changes in free energy can be computed with an error bar of typically 6 kcal/mol, such circumstances are much more favorable to atomistic simulations than changes in time constants of 1 order of magnitude, which correspond to free energy differences of only a few kcal/mol.

5. CONCLUSIONS

In conclusion, we have investigated the temperature dependence of vibrational energy transport from water surrounding myoglobin to a CO molecule in the Xe4 binding pocket at the center of the protein. The hindered rotational motion of the CO molecule, which is not covalently bound, results in a very sensitive response of its IR line-shape to temperature.^{16,17} Compared to previous work,^{10–14} where we have used anharmonic frequency shifts of protein backbone C=O modes as a signature of local temperature, the mechanism of this thermometer is more direct and better understood.

We observed a 4-fold acceleration of the CO response to mid-IR laser heating of the solvent between 20 and 70 K, in contrast to heat transport theory for proteins, which predicts a decrease of the thermal diffusivity with increasing temperature. Molecular dynamics simulations could also not reproduce the observed trend.

While it is at present not possible to provide a final answer as to why the simulations could not quantitatively describe heat transfer from the surroundings to the CO molecule, a number of factors can be excluded. We found experimentally that the thermalization of the solvent itself is not rate-limiting. The thermal properties of the protein and surrounding glycerol/water mixture are very similar with strongly overlapping density of states. Thus, this boundary does not appear to be rate-limiting either. Heat transport through the glycerol/water mixture (a glass) as well as the protein are expected to actually have an opposite temperature dependence, according to a theory developed by Leitner.^{35–37} The MD simulation agrees with this result, when taking into account that the latter is a classical mechanics description. This leaves us with the coupling between the protein and the CO in its binding pocket as the only conceivable bottleneck for energy transport. This coupling is very likely anharmonic and hence is expected to be temperature-dependent, regardless of whether one treats the problem classically or quantum-mechanically. Along the same lines, the second slower phase of the thermalization of the protein, which we attributed to the IVR of high frequency modes of the protein that is indeed anharmonic in nature, shows the expected temperature dependence (Figure 4).

■ ASSOCIATED CONTENT

S Supporting Information. The calibration of the laser induced temperature jump and the solution of the diffusion equation for spherical boundary conditions. This material is available free of charge via the Internet at <http://pubs.acs.org>.

■ AUTHOR INFORMATION

Corresponding Author

*E-mail: phamm@pci.uzh.ch (P.H.); M.Meuwly@unibas.ch (M.M.).

ACKNOWLEDGMENT

We thank David Leitner and Gerhard Stock for many inspiring discussions on the topic. This work has been supported by the Swiss National Science Foundation (Grant 200020-115877 and the NCCR MUST) as well as an ERC advanced investigator grant (DYNALLO) to P.H. Work in Basel was supported by the Swiss National Science Foundation (Grant 200020-132406 and the NCCR MUST), which is gratefully acknowledged. G.U.N. acknowledges funding from the Deutsche Forschungsgemeinschaft (Grant Ni291/3) and the CFN.

REFERENCES

- (1) Miller, R. J. D. *Annu. Rev. Phys. Chem.* **1991**, *42*, 581–614.
- (2) Lian, T.; Locke, B.; Kholodenko, Y.; Hochstrasser, R. M. *J. Phys. Chem.* **1994**, *98*, 11648–11656.
- (3) Li, P.; Champion, P. M. *Biophys. J.* **1994**, *66*, 430–436.
- (4) Mizutani, Y.; Kitagawa, T. *Science* **1997**, *278*, 443–445.
- (5) Henry, E. R.; Eaton, W. A.; Hochstrasser, R. M. *Proc. Natl. Acad. Sci. U.S.A.* **1986**, *83*, 8982–8986.
- (6) Ota, N.; Agard, D. A. *J. Mol. Biol.* **2005**, *351*, 345–354.
- (7) Sharp, K.; Skinner, J. J. *Proteins* **2006**, *65*, 347–361.
- (8) Kong, Y.; Karplus, M. *Proteins* **2008**, *74*, 145–154.
- (9) Sagnella, D. E.; Straub, J. E. *J. Phys. Chem. B* **2001**, *105*, 7057–7063.
- (10) Botan, V.; Backus, E. H. G.; Pfister, R.; Moretto, A.; Crisma, M.; Toniolo, C.; Nguyen, P. H.; Stock, G.; Hamm, P. *Proc. Natl. Acad. Sci. U.S.A.* **2007**, *104*, 12749–12754.
- (11) Backus, E. H. G.; Nguyen, P. H.; Botan, V.; Pfister, R.; Moretto, A.; Crisma, M.; Toniolo, C.; Stock, G.; Hamm, P. *J. Phys. Chem. B* **2008**, *112*, 9091–9099.
- (12) Backus, E. H. G.; Nguyen, P. H.; Botan, V.; Pfister, R.; Moretto, A.; Crisma, M.; Toniolo, C.; Zerbe, O.; Stock, G.; Hamm, P. *J. Phys. Chem. B* **2008**, *112*, 15487–15492.
- (13) Schade, M.; Moretto, A.; Donaldson, P. M.; Toniolo, C.; Hamm, P. *Nano Lett.* **2010**, *10*, 3057–3061.
- (14) Schade, M.; Moretto, A.; Crisma, M.; Toniolo, C.; Hamm, P. *J. Phys. Chem. B* **2009**, *113*, 13393–13397.
- (15) Nguyen, P. H.; Park, S.-M.; Stock, G. *J. Chem. Phys.* **2010**, *132*, 025102.
- (16) Kriegl, J. M.; Nienhaus, K.; Deng, P.; Fuchs, J.; Nienhaus, G. U. *Proc. Natl. Acad. Sci. U.S.A.* **2003**, *100*, 7069–7074.
- (17) Helbing, J.; Nienhaus, K.; Nienhaus, G. U.; Hamm, P. *J. Chem. Phys.* **2005**, *122*, 124505.
- (18) Hamm, P.; Kaindl, R. A.; Stenger, J. *Opt. Lett.* **2000**, *25*, 1798–1800.
- (19) Phillips, J. C.; Braun, R.; Wang, W.; Gumbart, J.; Tajkhorshid, E.; Villa, E.; Chipot, C.; Skeel, R. D.; Kale, L.; Schulten, K. *J. Comput. Chem.* **2005**, *26*, 1781–1802.
- (20) MacKerell, A. D., Jr.; Bashford, D.; Bellott, M.; Dunbrack, R. L., Jr.; Evanseck, J. D.; Field, M. J.; Fischer, S.; Gao, J.; Guo, H.; Ha, S.; Joseph-McCarthy, D.; Kuchnir, L.; Kucera, K.; Lau, F. T. K.; Mattos, C.; Michnick, S.; Ngo, T.; Nguyen, D. T.; Prodhom, B.; Reiher, W. E., III; Roux, B.; Schlenkrich, M.; Smith, J. C.; Stote, R.; Straub, J. E.; Watanabe, M.; Wiorkiewicz-Kuczera, J.; Yin, D.; Karplus, M. *J. Phys. Chem. B* **1998**, *102*, 3586.
- (21) Nutt, D. R.; Meuwly, M. *Proc. Natl. Acad. Sci. U.S.A.* **2004**, *101*, 5998–6002.
- (22) Jorgensen, W. L.; Chandrasekhar, J. D.; Madura, J. D.; Impey, R. W.; Klein, M. L. *J. Chem. Phys.* **1983**, *79*, 926.
- (23) Konishi, T.; Yanagita, T. *J. Stat. Mech.: Theory Exp.* **2009**, *09*, L09001.
- (24) Shirts, R. B.; Burt, S. R.; Johnson, A. M. *J. Chem. Phys.* **2006**, *125*, 164102.
- (25) Openov, L. A.; Podlivaev, A. I. *Phys. Solid State* **2008**, *50* (6), 1195–1200.
- (26) Uline, M. J.; Siderius, D. W.; Corti, D. S. *J. Chem. Phys.* **2008**, *128*, 124301.
- (27) Cheng, A.; Merz, K. *J. Phys. Chem.* **1996**, *100* (5), 1927–1937.
- (28) Talon, C.; Zou, Q. W.; Ramos, M. A.; Villar, R.; Vieira, S. *Phys. Rev. B* **2001**, *65*, 012203.
- (29) Andersson, O.; Johari, G. P.; Suga, H. *J. Chem. Phys.* **2004**, *120*, 9612–9617.
- (30) Lehle, H.; Kriegl, J. M.; Nienhaus, K.; Deng, P.; Fengler, S.; Nienhaus, G. U. *Biophys. J.* **2005**, *88* (3), 1978.
- (31) Lim, M.; Jackson, T. A.; Anfinrud, P. A. *J. Chem. Phys.* **1995**, *102*, 4355–4366.
- (32) Gordon, R. G. *J. Chem. Phys.* **1965**, *43*, 1307.
- (33) Devereux, M.; Meuwly, M. *J. Phys. Chem. B* **2009**, *113*, 13061–13070.
- (34) Sagnella, D. E.; Straub, J. E.; Jackson, T. A.; Lim, M.; Anfinrud, P. A. *Proc. Natl. Acad. Sci. U.S.A.* **1999**, *96*, 14324–14329.
- (35) Yu, X.; Leitner, D. M. *J. Phys. Chem. B* **2003**, *107*, 1698–1707.
- (36) Yu, X.; Leitner, D. M. *J. Chem. Phys.* **2005**, *122*, 054902.
- (37) Leitner, D. *Annu. Rev. Phys. Chem.* **2008**, *59*, 233–259.
- (38) Schade, M.; Hamm, P. *J. Chem. Phys.* **2009**, *131*, 044511.
- (39) Unsworth, J.; Duarte, F. J. *Am. J. Phys.* **1979**, *47* (11), 981–983.
- (40) Zeller, R. C.; Pohl, R. O. *Phys. Rev. B* **1971**, *4* (6), 2029.
- (41) Stock, G. *Phys. Rev. Lett.* **2009**, *102*, 118301.
- (42) Lee, M. W.; Meuwly, M. *J. Phys. Chem. B* **2011**, *115*, 5053–5061.